



Laser fabrication of Pt anchored Mo₂C micropillars as integrated gas diffusion and catalytic electrode for proton exchange membrane water electrolyzer

Haifeng Yuan^{a,1}, Lili Zhao^{a,1}, Bin Chang^{a,b}, Yuke Chen^a, Tianjiao Dong^a, Jietong He^a, Di Jiang^a, Wanqiang Yu^a, Hong Liu^{a,c,*}, Weijia Zhou^{a,**}

^a Collaborative Innovation Center of Technology and Equipment for Biological Diagnosis and Therapy in Universities of Shandong, Institute for Advanced Interdisciplinary Research (IAIR), University of Jinan, Jinan 250022, PR China

^b School of Chemistry and Chemical Engineering, University of Jinan, Jinan 250022, Shandong, PR China

^c State Key Laboratory of Crystal Materials, Shandong University, 27 Shandan Road, Jinan, Shandong 250100, PR China

ARTICLE INFO

Keywords:

Laser synthesis
Integrated electrode
Molybdenum carbide
Hydrogen evolution reaction
PEMWE electrolyzer

ABSTRACT

The efficient electrocatalysts for hydrogen evolution reaction (HER) are indispensable. Herein, Mo₂C micropillars decorated with Pt nanoparticles (<4 nm) on Mo foil (Pt/Mo₂C-L/Mo) are synthesized by laser ablation in a focused mode in CH₄ atmosphere and laser-induced reduction in an under-focused mode in Ar/H₂ atmosphere. The Pt/Mo₂C-L/Mo possesses excellent HER performance (21 mV at 10 mA cm⁻²) and stability (1317 mA cm⁻² for 100 h) in acid media. Integrated gas diffusion and catalytic electrodes of Pt/Mo₂C-L/Mo are constructed by laser in a mixed model and used in proton exchange membrane water electrolyzer (PEMWE). The voltage of the constructed PEMWE of (-) Pt/Mo₂C-L/Mo || IrO₂/Ti (+) (1.55 V at 10 mA cm⁻²) is lower than that of (-) 20 wt. % Pt/C || IrO₂ (+) (1.69 V at 10 mA cm⁻²) for overall water splitting. This work provides a universal laser synthetic strategy of integrated electrodes with promising application in the field of hydrogen energy.

1. Introduction

Hydrogen energy has the advantages of cleanliness and sustainability, and becomes one of the most likely candidates for fossil fuels [1,2]. As a simple approach to produce high-purity hydrogen, electrochemical water splitting has been extensively investigated [3–5]. However, the development of electrochemical water splitting for hydrogen production was limited by the abundant consumption of electrical energy. Therefore, the strategies to reduce electrical energy received extensive attention. The efficient electrocatalysts play an important role in decreasing the voltage of water splitting [6–9]. The metal platinum (Pt) and some other precious metals showed high hydrogen evolution reaction (HER) electrocatalytic activity. However, the high cost and shortage of precious metals limited their applications [10–12]. An effective strategy to reduce the load of precious metals without affecting HER efficiency was to aggrandize the specific surface area of precious metals.

Such as, Chen et al. synthesized monolayer Pt on transition metal carbides (TMCs) substrates which exhibited efficient HER performance comparable to that of bulk Pt [13]. In addition, TMCs possessed similar electronic structure to precious metals that facilitated electron transfer between Pt and TMCs substrates [14,15]. This not only exhibited acceleration influence on HER activity, but also improved the stability of Pt nanoparticles [16]. The researches of efficient electrocatalysts that coupled with precious metals and the low-cost TMCs had brought notable results [17,18]. As a result, TMCs were frequently used as electrocatalyst promoters. Notably, molybdenum carbides (Mo_xC_y) have superior stability and strong interaction with Pt, guaranteeing the long-term stability of the coupled catalysts [19–21]. This promising strategy not only effectively reduced the load of Pt, but also greatly improved the performance and stability of Pt/Mo_xC_y [22]. However, the conventional synthesis of Mo_xC_y required a high temperature above 800 °C, which was not conducive to industrial preparation [23–25]. In

* Corresponding author at: Collaborative Innovation Center of Technology and Equipment for Biological Diagnosis and Therapy in Universities of Shandong, Institute for Advanced Interdisciplinary Research (IAIR), University of Jinan, Jinan 250022, PR China.

** Corresponding author.

E-mail addresses: hongliu@sdu.edu.cn (H. Liu), ifc_zhouwj@ujn.edu.cn (W. Zhou).

¹ These authors contributed equally to this work

addition, these methods were difficult to achieve rapid heating/cooling. Furthermore, there was large excess heat wastage due to the sample volume being smaller than the heating volume of furnace. Therefore, the reliable and rapid synthesis strategies of Mo_xC_y at ambient temperature condition face serious challenges.

In recent years, the laser synthesis technology has gradually emerged and is considered as a promising strategy for the synthesis of electrocatalysts. The rapid development of laser synthesis technology was inseparable from the virtues of simple, time-saving, low energy consumption, controllable, environment-friendly and performed at ambient temperature condition [26,27]. The laser synthesis technique is based on the local photothermal reaction that derives from the absorption of irradiated laser by the target [28,29]. Zang et al. mentioned that the temperature generated by laser could reach 2000 K [30]. They had synthesized multiple transition metal carbides layers on glass substrate by preparing transition metallo-hydrogel firstly and following a CO_2 laser ablation process. In addition, laser technology could be utilized to construct micro/nanostructure. When the temperature was higher than the evaporation temperature of the material, the ablation effect occurred during the laser synthesis [31]. In this process, the melting of target and evaporating of massive ions, electrons, and atoms at the laser location were manifested, which could be utilized to construct the various micro/nanostructure. For example, Fan and Zhong et al. introduced micro/nanostructure on metal substrate via rapid laser ablation [32]. Therefore, the laser synthesis technology could realize the material synthesis and construction of micro/nanostructure.

With the virtues of high current densities, low ohmic loss, compact system design, fast system response and high stability, the proton exchange membrane water electrolyzer (PEMWE) was widely concerned and studied as an industrial electrolyzer [33,34]. The conventional PEMWE consisted of cathode collector, cathode porous transport layer, membrane electrode (Pt/C-PEM- IrO_2), anode porous transport layer and anode collector. However, the large number of components complicated the assembling process and increased the cost of electrolyzer. Therefore, the construction of integrated multifunctional electrode was a promising strategy to simplify the structure of electrolyzer. To realize such integrated multifunctional electrode, a laser processing technique might be a feasible strategy. Among the existing reports of laser processing of integrated electrode, In et al. constructed monofilament fiber supercapacitors by a laser synthesized strategy [35]. However, in the water splitting electrolyzer area, the current reports mainly focused on the laser preparation of catalysts [36,37], and the construction of the integrated electrodes and electrolyzer by laser still needed further work.

Herein, we presented the molybdenum carbide micropillars on Mo foil ($\text{Mo}_2\text{C-L/Mo}$) by focused laser ablation in CH_4 atmosphere at normal pressure and temperature, which realized the simultaneous formation of Mo_2C and construction of micropillars. Then, Pt nanoparticles anchored Mo_2C micropillars ($\text{Pt/Mo}_2\text{C-L/Mo}$) were synthesized by an under-focused laser method with the assistance of laser-induced reduction of platinum ions and the hydrophilicity of Mo_2C micropillars. The prepared $\text{Pt/Mo}_2\text{C-L/Mo}$ exhibited superior HER performance with an overpotential of 21 mV at 10 mA cm^{-2} and continuous stability for 100 h at high current density of 1317 mA cm^{-2} . Finally, an integrated gas diffusion and catalytic electrodes constructed by laser in a mixed model were employed in proton exchange membrane water electrolyzer ((-) $\text{Pt/Mo}_2\text{C-L/Mo}$ || IrO_2/Ti (+)), which represented excellent water splitting performance and were better than that of the commercial electrolyzer ((-) 20 wt.% Pt/C || IrO_2 (+)). In this work, the controllable laser synthesis and processing technologies of electrodes and electrolyzer for water splitting with high electrocatalytic performance and long-term durability have a bright application prospect in hydrogen energy field.

2. Experimental section

2.1. Chemicals

Chloroplatinic acid hexahydrate ($\text{H}_2\text{PtCl}_6 \cdot 6\text{H}_2\text{O}$), hexachloroiridium acid hydrate (H_2IrCl_6), and Nafion polymer dispersions D520 (5 wt.%) were bought from Shanghai Macklin Biochemical Co., Ltd. The concentrated sulfuric acid (H_2SO_4) and hydrochloric acid (HCl) were bought from Yantai Yuandong Fine Chemical Co., Ltd. High purity methane gas was purchased from Anqiu Hengan Gas Plant. Molybdenum and titanium foils were bought from Dahe New Energy Co., Ltd.

2.2. Laser ablation synthesis of molybdenum carbide micropillars on Mo foil ($\text{Mo}_2\text{C-L/Mo}$)

The purchased Mo foils were sonicated for 20 mins with 1 M hydrochloric acid solution, absolute alcohol, and deionized water, respectively. Using treated Mo foils as substrate, the structured Mo_2C micropillars ($\text{Mo}_2\text{C-L/Mo}$) were synthesized by a fiber laser in a CH_4 atmosphere at ambient pressure and temperature conditions. The laser system was LSF20D (Hgtech Laser). The model of the laser was YLP-1-100-20-20-HC-RG. The according wavelength and pulse width were 1064 nm and 100 ns. The single pulse energy of 1 mJ, repetition rate of 20 kHz, and scanning speed of 500 mm s^{-1} were implemented. The high-energy circular array (50 μm in diameter and spacing) procedure of laser in a focused mode with large average power of 19 W was used seven times for the laser synthesis of molybdenum carbide micropillars on Mo foil. The purposes of using the intense laser energy mode (a focused laser with large average power of 19 W) were twofold, to etch the micropillars and to utilize the resulting thermal effect for the synthesis of molybdenum carbide. For the laser ablation synthesis of $\text{Mo}_2\text{C-L/Mo}$ with the size of 5 mm * 5 mm, a time of 318 s was used.

2.3. Laser-induced reduction of platinum ions on the surface of molybdenum carbide micropillars for the synthesis of $\text{Pt/Mo}_2\text{C-L/Mo}$

The as-prepared Mo_2C micropillars on Mo foil ($\text{Mo}_2\text{C-L/Mo}$) with the size of 5 mm * 5 mm was firstly immersed in 1 mL 2×10^{-3} M H_2PtCl_6 solution completely overnight, then the platinum ions adsorbed on the surface of Mo_2C micropillars ($\text{Pt}^{4+}/\text{Mo}_2\text{C-L/Mo}$). The volume of H_2PtCl_6 solution used for the preparation of large-area size electrodes increased as area size increasing. For the reduction reaction of platinum ions, $\text{Pt}^{4+}/\text{Mo}_2\text{C-L/Mo}$ was processed by laser-assisted process under Ar/H_2 atmosphere. During this laser reduction process, the under-focused laser with weak average power of 7 W and scanning speed of 100 mm s^{-1} was conducted. Different from the focused laser used for the synthesis of molybdenum carbide micropillars, the under-focused laser for the laser reduction reaction produced only weak thermal effect for the reduction of platinum ions. In addition, the narrowest scanning spacing of 0.001 mm was set for the reduction reaction. For the laser-induced reduction of platinum ions on the surface of $\text{Mo}_2\text{C-L/Mo}$ with the size of 5 mm * 5 mm, a time of 261 s was used.

2.4. Characterization

The SEM images and elements mapping images were characterized by a field emission scanning electron microscope (FESEM, HITACHI regulus 8100). HRTEM images and elemental mapping images were carried out (Thermo Fischer Talos F200x). Moreover, the crystal structure was performed by XRD (Rigaku Ultima IV, JPN, $\lambda = 0.15406$ nm) with Cu K α radiation. The chemical analyses of the samples were conducted by XPS (AXIS SUPRA, Kratos). Inductively Coupled Plasma Optical Emission Spectrometer (ICP-OES, ICP-OES730, Agilent) was implemented for the calculation of Pt content. The temperatures in the experiments processes were characterized by Thermal Imaging Camera (Fotric 226) and infrared heat probe (IRTJ, Shanghai Electric Co., LTD).

Contact angle measuring instrument (JC2000D2G) was used for the contact angle measurements.

2.5. Electrochemical measurements

The electrochemical workstation (CHI 760E) was used on a three-electrode configuration for characterizing the catalytic activity of prepared samples. The working electrodes were as-prepared samples, and the electrolyte was 0.5 M H₂SO₄. The selective reference electrode was Ag/AgCl. An inactive and conductive carbon rod served as counter electrode. The sweeping potential from 0 V to −2 V for HER and from 0 V to 2 V for OER were conducted in the linear sweep voltammetry (LSV) tests. A slowly sweep rate of 5 mV s^{−1} was set in LSV testing. To calculate the efficient electrochemical active area (ECSA), the cyclic voltammetry (CV) tests were set in non-faradaic potential range. Electrochemical impedance spectroscopy (EIS) was performed. According frequency range was 0.01–100 kHz, and the amplitude was 10 mV. The current-time (i-t) testing was performed for a long period to research the durability of catalysts.

For the powder-like materials, such as 20 wt.% Pt/C and IrO₂, the according catalysts inks were prepared before electrochemical measurements. 2.5 mg material was added to 500 μL mixed solution. This solution consisted of H₂O, ethanol, and Nafion polymer dispersions with the volume ratio of 10: 9: 1. After the ultrasonication for 20 mins, a certain volume of ink was dispersed on glassy carbon electrode (0.07 cm²). For obtaining 20 wt.% Pt/C and IrO₂ electrodes with the same Pt and Ir loads per unit area as Pt/Mo₂C-L/Mo (0.359 mg_{Pt} cm^{−2}) and IrO₂/Ti (1 mg_{IrO₂} cm^{−2}) respectively, the 25 μL of 20 wt.% Pt/C ink and 14 μL of IrO₂ ink were dripped on glassy carbon electrodes.

2.6. The two electrode electrolyzer of (−) Pt/Mo₂C-L/Mo || IrO₂/Ti (+)

Utilizing Pt/Mo₂C-L/Mo as cathode electrode and IrO₂/Ti as anode electrode, a two-electrode electrolyzer of (−) Pt/Mo₂C-L/Mo || IrO₂/Ti (+) was assembled. The working electrode was connected with IrO₂/Ti, while both the reference electrode and counter electrode were connected with Pt/Mo₂C-L/Mo. A scanning speed of 5 mV s^{−1} and a sweeping potential range of 0–3 V were used in the polarization curves.

The integrated gas diffusion and catalytic electrodes were constructed by laser in a mixed model. To be precise, a circular array mode of laser (circular diameter of 500 μm and spacing of 800 μm) with high average power of 20 W was applied to the Ti foil and Mo foil for 30 mins, and the Ti and Mo collectors with porous structure were firstly obtained. After the synthesis of Pt/Mo₂C-L/Mo with micropillars structure on Mo collector, the integrated gas diffusion and catalytic electrodes of Pt/Mo₂C-L/Mo was obtained. Similarly, the integrated IrO₂/Ti electrode was synthesized by using porous Ti collector as substrate. Finally, the proton exchange membrane water electrolyzer (PEMWE) of (−) Pt/Mo₂C-L/Mo || IrO₂/Ti (+) was constructed with the integrated electrodes of Pt/Mo₂C-L/Mo and IrO₂/Ti, as well as proton membrane (NRE 212, Dupont) to form a sandwich construction. For establishing the proton exchange membrane water electrolyzer of (−) 20 wt.% Pt/C || IrO₂ (+), the catalyst-inks of 20 wt.% Pt/C (0.359 mg_{Pt} cm^{−2}) and IrO₂ (1 mg_{IrO₂} cm^{−2}) were sprayed on both sides of proton membrane followed a simultaneous heating of 120 °C and pressurization process of 0.5 MPa pressure for 30 mins. The laser-constructed Ti and Mo collectors with porous structure were sandwiched on both sides of the proton membrane containing IrO₂ and 20 wt.% Pt/C. Then a proton exchange membrane water electrolyzer of (−) 20 wt.% Pt/C || IrO₂ (+) was obtained finally.

2.7. DFT calculations method

The Vienna ab initio simulation package (VASP) was applied in all the spin-polarized computations [38,39]. The projector augmented wave was utilized to illustrate the mutual effect between ions and

electrons [40]. The general gradient approximation was adopted for Perdew-Burke-Ernzerhof (PBE) form [41,42]. Optimized structure model of a Pt₁₀ cluster stabilized on the 4 × 3 Mo₂C (100) slab was established. The convergence criterion of residual force and energy were 0.03 eV Å^{−1} and 10^{−5} eV for the structure relaxation. The sample model of Brillouin zones was employed on Monkhorst-Pack 2 × 2 × 1 k-point grid. It was a vacuum space of 15 Å that was used to avoid the interaction between two periodic units.

Generally, the free energy of hydrogen adsorption (ΔG_{H*}) was used to assess the performance of HER [43]. The formula was shown as below:

$$\Delta G_{H^*} = \Delta E + \Delta E_{ZPE} - T\Delta S$$

The ΔE and E_{ZPE} were the reaction energy difference and zero-point energies. And the T and S were temperature and entropy. Commonly, the value of |ΔG_{H*}| for an excellent HER catalyst is closer to zero.

3. Results and discussion

3.1. Catalyst synthesis

Herein, the synthesis of Pt/Mo₂C-L/Mo was performed by a controllable laser ablation, followed by laser reduction of platinum ions in ambient environment. As shown in Fig. S1a, the experimental apparatus for the synthesis of Pt/Mo₂C-L/Mo was a glass vessel, in which the specific gases could circulate. Precisely, as shown in Fig. 1a, utilizing Mo foil as substrate, the Mo₂C micropillars were obtained on Mo foil (Mo₂C-L/Mo) through laser ablation under a focused mode using circular array procedure in CH₄ atmosphere, which realized the simultaneous synthesis of Mo₂C and the construction of micropillars. In this process, the microscale Mo at the laser ablation position reacted with CH₄ to form Mo₂C, and some Mo particles were simultaneously sputtered out and evaporated to form the micropillars structure. Importantly, the strong laser energy mode (a focused laser with large average power of 19 W) was used to etch the micropillars structure and performed thermal effect for the synthesis of molybdenum carbide. After being immersed in H₂PtCl₆ solution overnight, the Pt⁴⁺ were distributed on the surface of Mo₂C micropillars (Pt⁴⁺/Mo₂C-L/Mo). Then the Pt nanoparticles on Mo₂C micropillars (Pt/Mo₂C-L/Mo) were eventually obtained by laser-induced reduction under Ar/H₂ atmosphere using an under-focused laser. Instead of a focused laser used for the synthesis of molybdenum carbide micropillars, an under-focused laser with weak average power of 7 W for the laser reduction reaction, which produced only weak thermal effect for the reduction of platinum ions.

Particularly, in the whole synthetic process of Pt/Mo₂C-L/Mo, the temperature at Mo foil except for the location of laser spot and the experimental apparatus maintained normal pressure and temperature. The temperature of the experimental apparatus in the two steps synthetic process were measured by the Thermal Imaging Camera (the right images of Fig. 1b, c). For the Thermal Imaging Camera, the infrared radiation energy of the measured target was received by an infrared detector. Then the infrared radiation energy distribution graph was reflected on the photosensitive elements, and the infrared thermal image was obtained. The different colors above the thermal image represent the different temperatures. As shown in the right images of Fig. 1b, c, the maximum temperatures of experimental apparatus during laser ablation synthesis and laser-induced reduction process were only 37 °C and 35 °C, respectively, while the ambient temperature was close to room temperature. During the synthetic process of Pt/Mo₂C-L/Mo, the temperature on Mo foil except for the location of laser spot was ambient temperature and the Mo foil could even be touched (Fig. S1b). To measure the temperature of laser spot, an infrared heat probe was used. As shown in the left image of Fig. 1b, the general temperature of experimental apparatus in laser ablation synthesis of Mo₂C-L/Mo was 873 °C, which was similar to the temperature used for the conventional

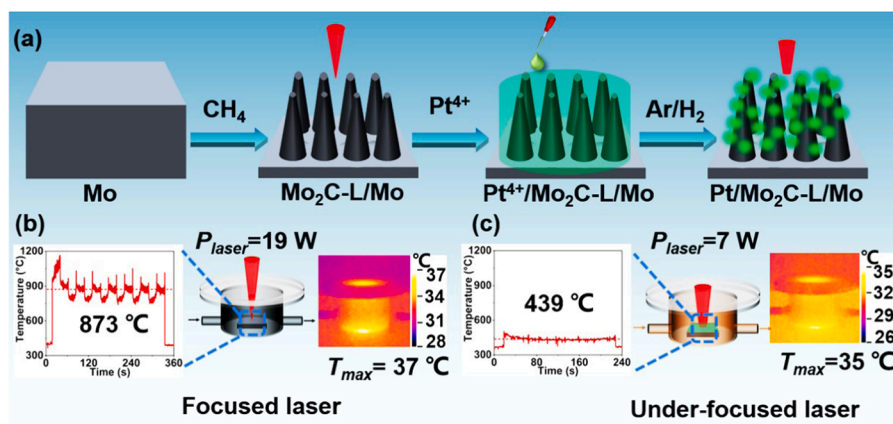


Fig. 1. (a) Illustration of the laser synthetic process of Pt/Mo₂C-L/Mo. Experimental apparatus and according temperature images of (b) the laser ablation synthesis of Mo₂C-L/Mo with focused laser and (c) the laser-induced reduction process of Pt/Mo₂C-L/Mo with under-focused laser.

synthesis of molybdenum carbide in previous reports [44–46]. In the laser-induced reduction process of Pt/Mo₂C-L/Mo, a general temperature of 439 °C was performed (the left image of Fig. 1c), which was auxiliary for the reduction of Pt⁴⁺ [47,48]. The difference of temperatures in laser ablation synthesis of Mo₂C-L/Mo and the laser-induced

reduction process of Pt/Mo₂C-L/Mo was due to the power of the laser. Therefore, throughout the synthesis of Pt/Mo₂C-L/Mo, the Mo foil except for the location of laser spot and the experimental apparatus maintained normal temperature, and the high temperatures only presented at laser spot for driving both reactions. For comparison, the

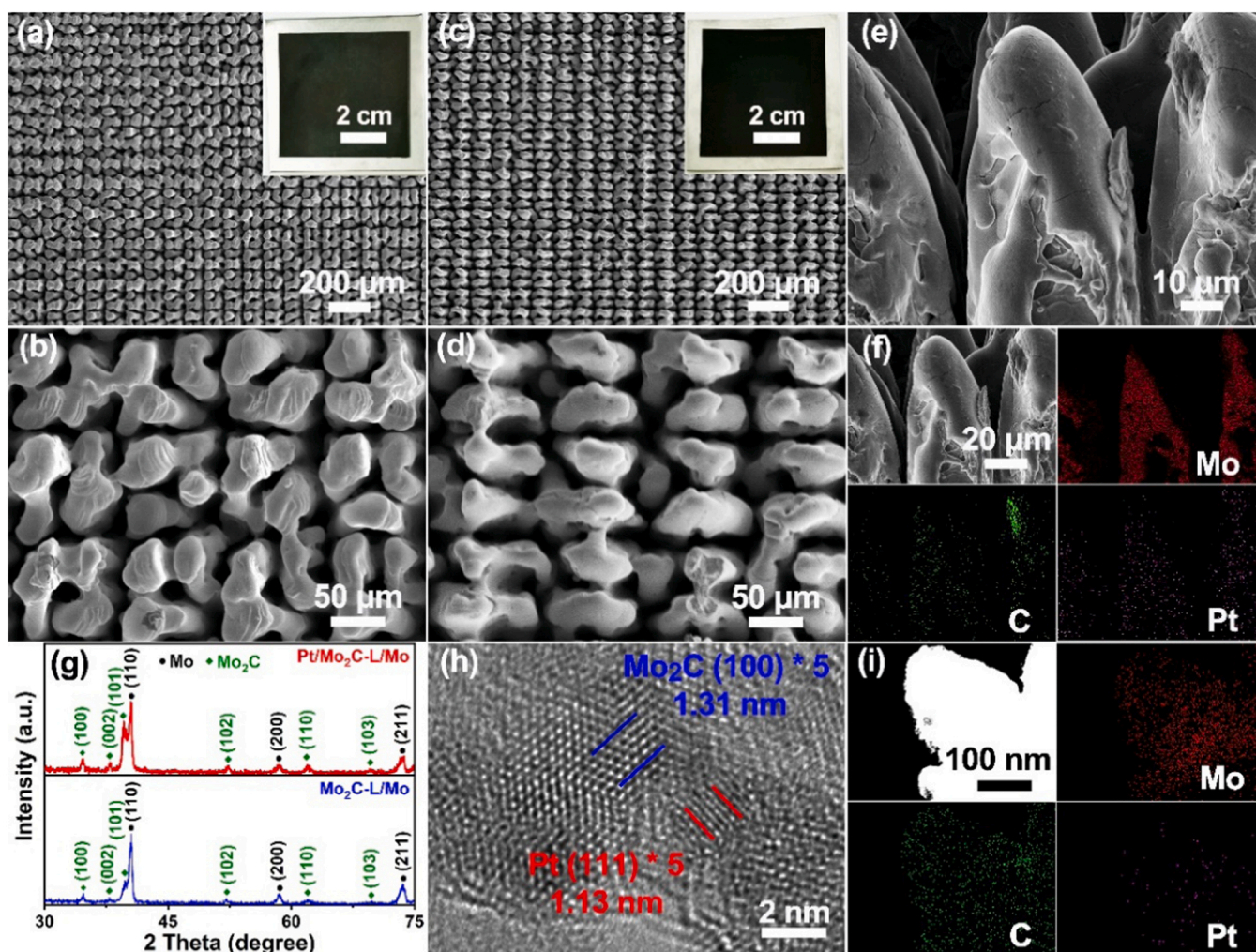


Fig. 2. SEM images of (a, b) Mo₂C-L/Mo and (c, d) Pt/Mo₂C-L/Mo. Insets were the digital images of Mo₂C-L/Mo and Pt/Mo₂C-L/Mo in large size. (e) The side view and (f) according elements mapping of Pt/Mo₂C-L/Mo. (g) XRD patterns of Mo₂C-L/Mo and Pt/Mo₂C-L/Mo. (h) HRTEM image and (i) according EDS mapping of Pt/Mo₂C-L.

molybdenum carbide on Mo foil ($\text{Mo}_2\text{C-HTC/Mo}$) was synthesized by the traditional high-temperature calcination (1000°C , 120 mins) in CH_4 atmosphere in a furnace (synthesis details in [Supporting Information](#)). According synthetic illustration was shown in [Fig. S2](#). The successful synthesis of $\text{Mo}_2\text{C-HTC/Mo}$ was demonstrated by the XRD pattern ([Fig. S3](#)). In addition, both of the energy consumption ($6.0 \times 10^3 \text{ J}$) and synthesis time ($\sim 5 \text{ mins}$) of $\text{Mo}_2\text{C-L/Mo}$ were much lower than those of $\text{Mo}_2\text{C-HTC/Mo}$ ($1.7 \times 10^6 \text{ J}$, 120 mins) (calculation details in [Supporting Information](#)). Therefore, the comparison between traditional high-temperature calcination method and laser synthesis strategy manifested that the high energy consumption was avoided, and the synthesis time was greatly shortened in laser synthesis process.

3.2. Catalyst structure characterizations

Using the laser ablation of Mo foil substrate in CH_4 atmosphere, Mo_2C micropillars ($\text{Mo}_2\text{C-L/Mo}$) were generated ([Fig. 2a](#)). By enlarging the image of $\text{Mo}_2\text{C-L/Mo}$, the micropillars morphology could be clearly observed ([Fig. 2b](#)). After laser reduction of Pt^{4+} on Mo_2C micropillars, the micropillars morphology of obtained $\text{Pt/Mo}_2\text{C-L/Mo}$ inherited from $\text{Mo}_2\text{C-L/Mo}$ ([Fig. 2c, d](#)). Owing to the scalability of laser synthesis, the large-size of $\text{Mo}_2\text{C-L/Mo}$ and $\text{Pt/Mo}_2\text{C-L/Mo}$ with the size of $6 \text{ cm} \times 6 \text{ cm}$ were synthesized (inset of [Fig. 2a, c](#)), which demonstrated the potential for industrial applications. Particularly, the side views of $\text{Pt/Mo}_2\text{C-L/Mo}$ showed the micropillars with the diameter of $40\text{--}60 \mu\text{m}$ and the height of $200 \mu\text{m}$ ([Fig. 2e-f](#) and [S4](#)). Interestingly, attributed to the controllable characteristic of laser synthesis technology, the density of micropillars on Mo foil could be controlled by changing the spacing and diameter of the circles in circular array procedure for laser synthesis process. As shown in [Fig. S5](#), the $\text{Pt/Mo}_2\text{C-L/Mo}$ with different density of micropillars (micropillars spacing of $30 \mu\text{m}$, $50 \mu\text{m}$, $80 \mu\text{m}$, and $100 \mu\text{m}$) were prepared.

The XRD pattern of $\text{Mo}_2\text{C-L/Mo}$ in [Fig. 2g](#) showed that, apart from the representative peaks at 40.5° , 58.6° , and 73.7° attributed to (110), (200) and (211) crystal planes of metallic Mo (JCPDS no. 42–1120), the typical diffraction peaks at 34.4° , 38.0° , 39.4° , 52.1° , 61.5° , and 69.6° attributed to (100), (002), (101), (102), (110), and (103) crystal planes were distinguished as hexagonal Mo_2C (JCPDS no. 35–0787) (referred as $\beta\text{-Mo}_2\text{C}$ [49]), implying the successful reaction between CH_4 and Mo substrate during laser ablation process. While from the XRD pattern of $\text{Pt/Mo}_2\text{C-L/Mo}$ in [Fig. 2g](#), the Pt peaks did not appear that might be due to the low loading amount of Pt, which was similar to previous report [50]. In order to identify the reduction of Pt, the elements mapping of $\text{Pt/Mo}_2\text{C-L/Mo}$ in side views were performed and the uniform distribution of Pt element on the surface of micropillars was clearly shown ([Fig. 2f](#) and [S4](#)), confirming the Pt nanoparticles with super small size were uniformly loaded on the $\text{Mo}_2\text{C-L/Mo}$ by laser. The ICP-OES of $\text{Pt/Mo}_2\text{C-L/Mo}$ was implemented and the Pt loading amount was $0.359 \text{ mgPt cm}^{-2}$. At last, XPS analyses were processed to understand the composition and valence state of $\text{Mo}_2\text{C-L/Mo}$ and $\text{Pt/Mo}_2\text{C-L/Mo}$ ([Fig. S6](#)). The full XPS spectrum of $\text{Mo}_2\text{C-L/Mo}$ showed elements signals of Mo, C, and O, while $\text{Pt/Mo}_2\text{C-L/Mo}$ showed elements signals of Mo, C, O, and Pt ([Fig. S6a](#)). These results were auxiliary in confirming the successful preparation of $\text{Mo}_2\text{C-L/Mo}$ and $\text{Pt/Mo}_2\text{C-L/Mo}$ [49]. The high-resolution XPS spectra of Mo 3d for $\text{Mo}_2\text{C-L/Mo}$ was distinguished to six peaks ([Fig. S6b](#)). The Mo^{2+} with peaks at 228.45 eV ($\text{Mo } 3d_{5/2}$) and 231.64 eV ($\text{Mo } 3d_{3/2}$) could be assigned to Mo-C in $\text{Mo}_2\text{C-L/Mo}$. In addition, the high-valence-state Mo species, Mo^{4+} ($\text{Mo } 3d_{5/2}$ at 229.31 eV , $\text{Mo } 3d_{3/2}$ at 234.29 eV) and Mo^{6+} ($\text{Mo } 3d_{5/2}$ at 232.56 eV , $\text{Mo } 3d_{3/2}$ at 235.65 eV) could be due to the inevitable partial oxidation of the surface of $\text{Mo}_2\text{C-L/Mo}$ when being exposed to air [51]. In addition, the XPS spectra of Pt 4f for $\text{Pt/Mo}_2\text{C-L/Mo}$ was identified ([Fig. S6c](#)), and the peaks of Pt^0 ($\text{Pt } 4f_{7/2}$ at 71.50 eV , $\text{Pt } 4f_{5/2}$ at 74.80 eV) was revealed, confirming the successful reduction of Pt^{4+} by laser [52]. After the loading of Pt, the negative shift of Mo^{2+} ($\text{Mo } 3d_{5/2}$ at 227.75 eV , $\text{Mo } 3d_{3/2}$ at 231.01 eV) for $\text{Pt/Mo}_2\text{C-L/Mo}$ was revealed,

which was probably owing to the bonding between Mo and Pt [53]. For the HRTEM measurement of $\text{Pt/Mo}_2\text{C-L}$, the $\text{Pt/Mo}_2\text{C-L}$ was scraped from Mo foil substrate, dispersed in anhydrous ethanol, and dripped on a copper net. The lattice spacing of 0.261 nm was attributed to the (100) plane of Mo_2C ([Fig. 2h](#)). And the lattice spacing of 0.226 nm could be attributed to the (111) plane of Pt and this result confirmed the successful loading of Pt on the surface of $\text{Mo}_2\text{C-L}$ [49]. As shown in [Fig. S7](#), the size distribution range of Pt nanoparticles was $< 4 \text{ nm}$, confirming the constraining effect of Mo_2C micropillars as substrate and the rapid nucleation growth of Pt via the laser reduction. In addition, the interface of Pt and Mo_2C (marked by red dotted line in [Fig. S7](#)) existed and this result confirmed the existence of combination of Pt and Mo_2C . The according EDS mapping of the $\text{Pt/Mo}_2\text{C-L}$ revealed the uniform distribution of Mo, C, and Pt elements ([Fig. 2i](#)).

3.3. Surface structure and properties of catalyst

The hydrophilicity on the surface of $\text{Mo}_2\text{C-L/Mo}$ micropillars substrate played an important role for the adsorption of Pt^{4+} aqueous solution, which allowed for regionally selective synthesis of Pt nanoparticles. The SEM image showed the obvious interface between Mo (the left) and $\text{Mo}_2\text{C-L/Mo}$ micropillars (the right, highlighted in red) ([Fig. 3a](#)). To verify the hydrophilicity of Mo and $\text{Mo}_2\text{C-L/Mo}$ substrates, a series of surface contact angle tests were performed. When the sessile drop contact angle tests were implemented using droplet of $0.5 \mu\text{L}$ H_2PtCl_6 solution, the contact angle of $\text{Mo}_2\text{C-L/Mo}$ was 0° indicating the super hydrophilic property of $\text{Mo}_2\text{C-L/Mo}$, while the contact angle of Mo was 76.44° manifesting that it had the relatively hydrophobic surface ([Fig. 3b, c](#)). Interestingly, a local $\text{Mo}_2\text{C-L}$ micropillars sample with the size of 1 mm^2 on Mo foil (named $\text{Mo}|\text{Mo}_2\text{C-L}|\text{Mo}$) was prepared, and a series of sessile drop contact angle measurements in different amounts of droplets were performed ([Fig. 3d](#) and [S8](#)). As the droplet mass increased from $0.3 \mu\text{L}$ to $1.3 \mu\text{L}$, the surface of $\text{Mo}_2\text{C-L}$ micropillars with the size of 1 mm^2 was wrapped completely in droplet ([Fig. 3d](#)). The water accumulated at the position of $\text{Mo}_2\text{C-L}$ micropillars and did not overflow the boundary between the $\text{Mo}_2\text{C-L}$ and Mo, which was credited to the hydrophilicity of $\text{Mo}_2\text{C-L}$ and relative hydrophobicity of Mo substrate. The dynamic sessile drop contact angle measurement at the interface between Mo and $\text{Mo}_2\text{C-L}$ micropillars ($\text{Mo}|\text{Mo}_2\text{C-L}$) was also carried out ([Fig. 3e](#)). The spontaneous tilt and movement of the droplet strongly demonstrated that the surface of $\text{Mo}_2\text{C-L}$ was more hydrophilic than that of Mo. In addition, in [Fig. 3f](#), the flow conditions of $2 \mu\text{L}$, $4 \mu\text{L}$, and $6 \mu\text{L}$ rhodamine B aqueous solution in rectangular channel of $\text{Mo}_2\text{C-L}$ micropillars on Mo foil ($\text{Mo}_2\text{C-L/Mo}$) were clearly observed by fluorescence microscope, giving compelling evidence for the solution flow on the hydrophilic surface of $\text{Mo}_2\text{C-L/Mo}$. As a comparison, the sessile drop contact angle measurement of $\text{Mo}_2\text{C-HTC/Mo}$ with plane structure (SEM image in [Fig. S9a](#)) was implemented using droplet of $0.5 \mu\text{L}$ H_2PtCl_6 solution. The contact angle of $\text{Mo}_2\text{C-HTC/Mo}$ was 90.48° , which illustrated the hydrophobic surface property ([Fig. S9b](#)). Therefore, the hydrophilicity of $\text{Mo}_2\text{C-L/Mo}$ prepared by laser process was mainly due to the micropillars structure [54]. Owing to the hydrophilic property of $\text{Mo}_2\text{C-L/Mo}$ micropillars, the easier ions adsorption was reliable for the reduction process of Pt^{4+} by laser for the synthesis of $\text{Pt/Mo}_2\text{C-L/Mo}$. Benefiting from the flexibility and scalability of laser synthesis as well as hydrophilic property of $\text{Mo}_2\text{C-L/Mo}$ micropillars, the $\text{Pt/Mo}_2\text{C-L/Mo}$ in a variety of patterns and sizes were also designed as expected. As shown in [Fig. 3g-i](#), the $\text{Pt/Mo}_2\text{C-L/Mo}$ with particular designability of patterns including letters of UJN, bear head, and square column array were prepared.

3.4. HER catalytic performance

The electrocatalytic HER activities of $\text{Mo}_2\text{C-L/Mo}$, $\text{Pt/Mo}_2\text{C-L/Mo}$, $20 \text{ wt.}\% \text{ Pt/C}$, and $\text{Mo}_2\text{C-HTC/Mo}$ were performed in $0.5 \text{ M H}_2\text{SO}_4$. The structure characterizations and details of the commercial $20 \text{ wt.}\% \text{ Pt/C}$

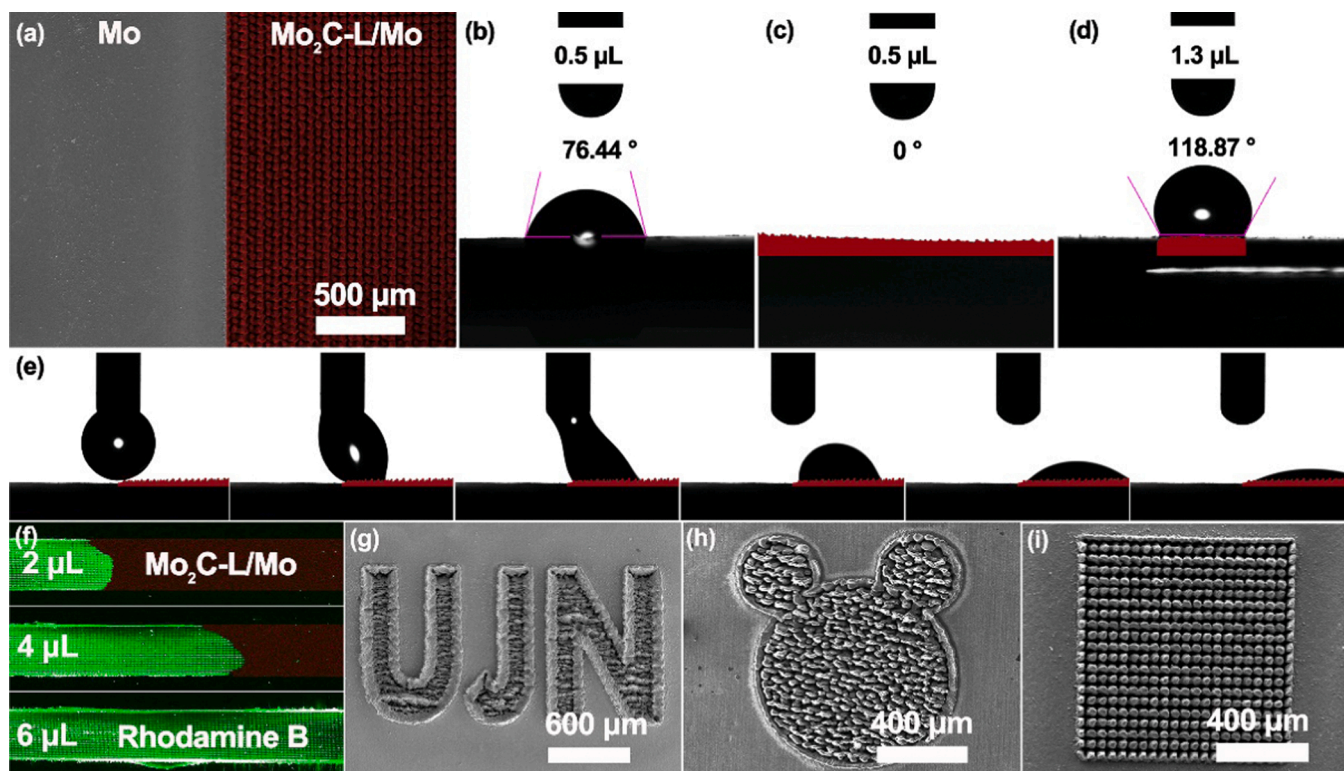


Fig. 3. (a) SEM image of the interface between Mo (the left) and Mo₂C-L/Mo micropillars (the right, highlighted in red). The surface contact angle measurements of the (b) Mo, (c) Mo₂C-L/Mo using droplet of 0.5 μL H₂PtCl₆ solution, and (d) Mo|Mo₂C-L/Mo with the size of 1 mm² for local Mo₂C-L micropillars using droplet of 1.3 μL H₂PtCl₆ solution. (e) The dynamic sessile drop contact angle measurement at the interface between Mo and Mo₂C-L (named Mo|Mo₂C-L) using droplet of 0.5 μL H₂PtCl₆ solution. (f) Microscope images of the flow of rhodamine B aqueous solution in rectangular Mo₂C-L/Mo. (g-i) SEM images of Pt/Mo₂C-L/Mo with various patterns.

catalyst were exhibited in Fig. S10 in Supporting Information. Note that the Mo₂C-L/Mo, Pt/Mo₂C-L/Mo, and Mo₂C-HTC/Mo catalysts were synthesized on Mo foil substrate, so they were self-standing and binder-free electrodes. As shown in Fig. 4a, the HER polarization curves demonstrated that the overpotential (η_{10} , an overpotential at 10 mA cm⁻²) of Mo₂C-L/Mo was 214 mV, which was much lower than that of Mo₂C-HTC/Mo (326 mV), due to the micropillars array with the hydrophilic property (Fig. 3c and S9b). More importantly, the Pt/Mo₂C-L/Mo required only 21 mV at 10 mA cm⁻² and 993 mV at 1000 mA cm⁻². The 20 wt.% Pt/C with the same Pt load of 0.359 mg_{Pt} cm⁻² needed larger overpotentials (25 mV at 10 mA cm⁻² and 1199 mV at 1000 mA cm⁻²) than Pt/Mo₂C-L/Mo. These might be due to that the substrate of Mo₂C-L/Mo micropillars array had larger specific surface area and hydrophilic surface for promoting the better dispersion of Pt nanoparticles. Therefore, these contrastive results demonstrated the appealing HER performance of the Pt/Mo₂C-L/Mo at high current densities and the possibility of industrial application. In order to explore the reduction effect of the thermal generated by laser and Ar/H₂ atmosphere for Pt⁴⁺, the samples were prepared with the process of an under-focused laser under Ar/H₂ (Pt/Mo₂C-L/Mo-Ar/H₂) and Ar atmosphere (Pt/Mo₂C-L/Mo-Ar). As shown in the polarization curves for HER (Fig. S11), the current density of Pt/Mo₂C-L/Mo-Ar was smaller than Pt/Mo₂C-L/Mo-Ar/H₂. Compared Pt/Mo₂C-L/Mo-Ar with Pt/Mo₂C-L/Mo-Ar/H₂, the reduction effect of the Ar/H₂ atmosphere for Pt⁴⁺ was demonstrated. Therefore, both thermal generated by laser and Ar/H₂ atmosphere were indispensable for the reduction of Pt⁴⁺.

To further explore the intrinsic property of the catalysts and the efficiency of the catalytic reaction, the Tafel slopes and exchange current density (j_0) of all samples were investigated. The Tafel slope value of Pt/Mo₂C-L/Mo (43.7 mV dec⁻¹) was smaller than that of Mo₂C-L/Mo (65.0 mV dec⁻¹) and Mo₂C-HTC/Mo (65.9 mV dec⁻¹) (Fig. 4b). This

result proved that Pt/Mo₂C-L/Mo had a faster HER kinetics. As the Tafel slope value of Pt/Mo₂C-L/Mo was slightly bigger than 40 mV dec⁻¹, HER reaction process was likely to be Volmer-Heyrovsky reaction route and the electrochemical desorption step (Heyrovsky reaction) might be the rate-determining step [55–57]. In addition, the exchange current density (j_0) of Mo₂C-L/Mo (0.16 mA cm⁻²) was higher than that of Mo₂C-HTC/Mo (0.12 mA cm⁻²), proving the better HER activity of Mo₂C-L/Mo than Mo₂C-HTC/Mo (Fig. S12a). The j_0 of Pt/Mo₂C-L/Mo (3.70 mA cm⁻²) was higher than that of 20 wt.% Pt/C (2.94 mA cm⁻²), indicating the better HER activity of Pt/Mo₂C-L/Mo (Fig. S12a). The turnover frequency (TOF) represented the change of the number of reactant molecules on per active site in unit time. It was well known that the larger TOF value indicated the higher catalytic activity [58–60]. The TOF was computed for further exploring the intrinsic HER performance of Pt/Mo₂C-L/Mo and 20 wt.% Pt/C (Fig. S12b). In particular, the TOF value of Pt/Mo₂C-L/Mo at 150 mV (vs. RHE) was 0.86 H₂ s⁻¹, which was slightly higher than that of 20 wt.% Pt/C (0.76 H₂ s⁻¹). EIS Nyquist plots of Mo₂C-L/Mo, Pt/Mo₂C-L/Mo, 20 wt.% Pt/C, and Mo₂C-HTC/Mo for HER were shown in Fig. 4c. As shown, the charge transfer resistance (R_{ct}) of Pt/Mo₂C-L/Mo (4.6 Ω) was smaller than that of Mo₂C-HTC/Mo (17.1 Ω), Mo₂C-L/Mo (12.1 Ω), and 20 wt.% Pt/C (5.1 Ω) with a same overpotential of 250 mV. Indicating the fastest HER reaction kinetics was occurred at the interface of Pt/Mo₂C-L/Mo and electrolyte. Furthermore, the ECSA was utilized to characterize the number of active sites. The double-layer capacitance (C_{dl}) was acquired by using cyclic voltammetry testing (Fig. S13), which was proportional to the ECSA. As shown in Fig. 4d, the ECSA of Pt/Mo₂C-L/Mo (160.8 mF cm⁻²) was remarkable larger than that of Mo₂C-L/Mo (43.9 mF cm⁻²), 20 wt.% Pt/C (53.0 mF cm⁻²), and Mo₂C-HTC/Mo (1.6 mF cm⁻²), indicating the Pt/Mo₂C-L/Mo had more exposed active sites. Therefore, the successful reduction and loading of Pt nanoparticles of Pt/Mo₂C-L/Mo was

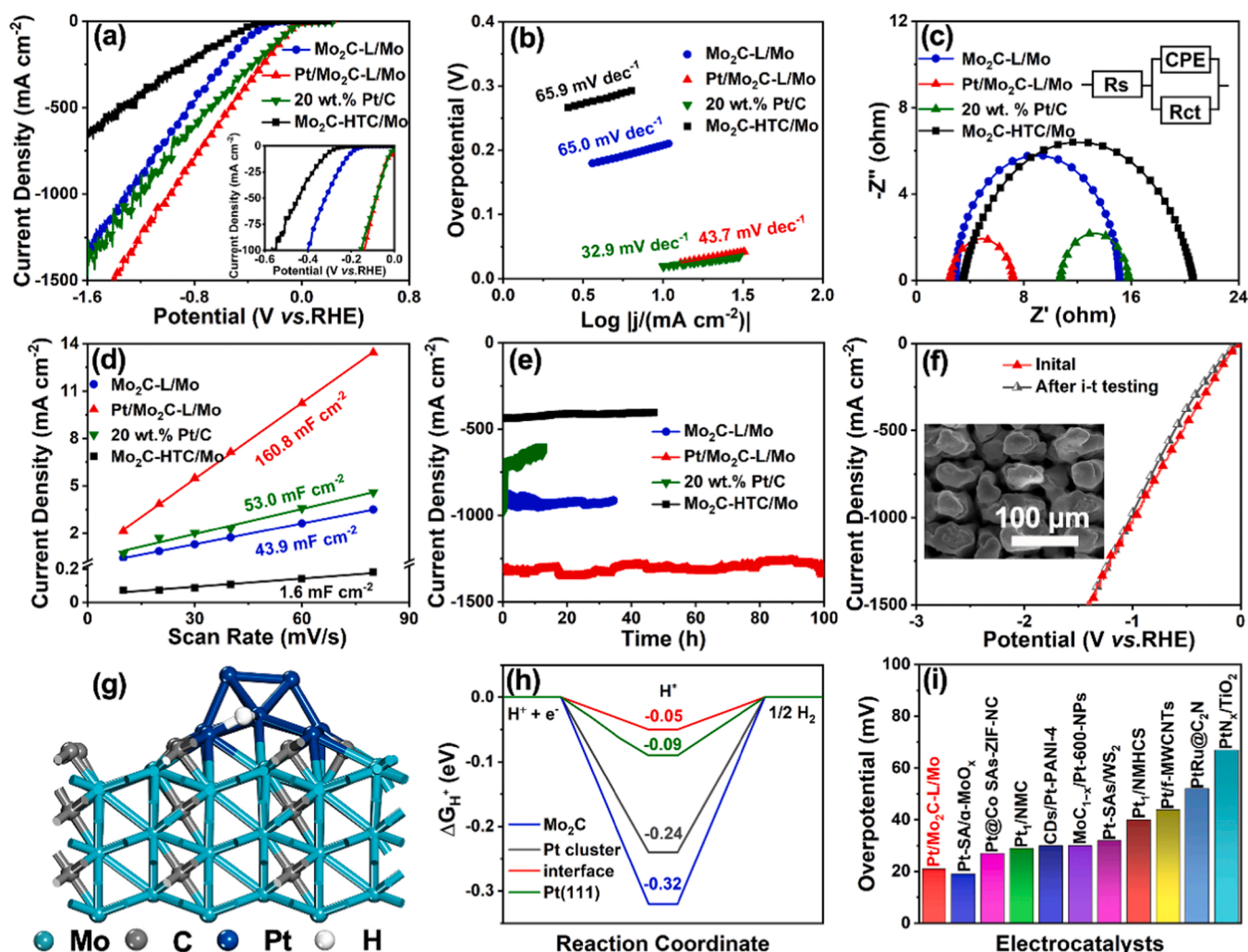


Fig. 4. (a) Polarization curves for HER (inset was detail drawing), (b) Tafel plots, (c) Nyquist plots (overpotential of 250 mV), (d) electrochemical surface area, and (e) current-time plots (overpotential of 1.22 V) of Mo₂C-L/Mo, Pt/Mo₂C-L/Mo, 20 wt.% Pt/C, and Mo₂C-HTC/Mo in 0.5 M H₂SO₄. (f) The polarization curves before and after i-t testing of Pt/Mo₂C-L/Mo. Inset was the SEM image of Pt/Mo₂C-L/Mo after i-t testing. (g) Optimized structure model of Pt cluster stabilized on the Mo₂C (100) for Pt/Mo₂C and hydrogen absorption site on the interface between Mo₂C (100) and Pt cluster. (h) Calculated free energy for H adsorption on Pt cluster, interface, and Mo₂C (100) surface sites of Pt/Mo₂C. (i) Comparison of the overpotential (η_{10} , an overpotential at 10 mA cm⁻²) of the reported Pt-based electrocatalysts for electrocatalytic HER activity.

indispensable for possessing the more active sites. The HER polarization curves corrected by ECSA of Mo₂C-L/Mo, Pt/Mo₂C-L/Mo, 20 wt.% Pt/C, and Mo₂C-HTC/Mo were shown in Fig. S14. The intensities of Pt/Mo₂C-L/Mo and 20 wt.% Pt/C were roughly the same at small overpotential, implying the Mo₂C-L/Mo micropillars substrate of Pt/Mo₂C-L/Mo was beneficial to the dispersion of Pt. In addition, the electrochemical surface area and polarization curves for HER of Pt/Mo₂C-L/Mo with different density of micropillars were conducted (Fig. S15). As shown in Fig. S15a, the 183.6 mF cm⁻², 160.8 mF cm⁻², 150.4 mF cm⁻², and 127.1 mF cm⁻² corresponded to the electrochemical surface area of Pt/Mo₂C-L/Mo with micropillars spacing of 30 μm , 50 μm , 80 μm , and 100 μm . The current density in polarization curves increased and the trend was more obvious at high potential (Fig. S15b). Therefore, as the increasing density of micropillars, the number of active sites and current density increased.

In addition, the stability at high current density of catalysts was indispensable for practical applications in hydrogen energy area. The high current density durability tests of Mo₂C-L/Mo, Pt/Mo₂C-L/Mo, 20 wt.% Pt/C, and Mo₂C-HTC/Mo were implemented at same overpotential of 1.22 V for continuous measurements (Fig. 4e). The Pt/Mo₂C-L/Mo (1317 mA cm⁻²) manifested the higher current density

than that of Mo₂C-L/Mo (913 mA cm⁻²), implying the reduction and loading of Pt on the surface of Mo₂C-L/Mo played an important role in contributing to the HER performance. It was noteworthy to mention that the current density of Pt/Mo₂C-L/Mo had $\sim 100\%$ retention after i-t testing at the high current density of 1317 mA cm⁻² for 100 h. In addition, the Pt/Mo₂C-L/Mo exhibited more preferable stability than that of 20 wt.% Pt/C ($\sim 62.9\%$ retention for 12 h) due to the electrode of Pt/Mo₂C-L/Mo without the Nafion binder. The current density of Mo₂C-L/Mo (913 mA cm⁻²) was higher than that of Mo₂C-HTC/Mo (441 mA cm⁻²), which could be attributed to the hydrophilic surface and micropillars structure constructed by laser for Mo₂C-L/Mo. Furthermore, the polarization curves of Mo₂C-L/Mo, Pt/Mo₂C-L/Mo, 20 wt.% Pt/C, and Mo₂C-HTC/Mo before and after the i-t testing were also conducted (Fig. 4f and S16). For Mo₂C-L/Mo and Pt/Mo₂C-L/Mo, the LSV curves before and after the i-t testing remained virtually unchanged (Fig. 4f and S16a), while there was obvious attenuation for 20 wt.% Pt/C after the i-t testing (Fig. S16b). Moreover, the SEM image presented the unbroken structure of Pt/Mo₂C-L/Mo after i-t testing (inset of Fig. 4f). The XRD, XPS, and HRTEM were also performed for the Pt/Mo₂C-L/Mo after i-t testing (Fig. S17), and these results were consistent with the characterization results before i-t testing of Pt/Mo₂C-

L/Mo. The correction of potential for Ag/AgCl reference after i-t testing of Pt/Mo₂C-L/Mo was conducted, in which the calibrated potential of 0.197 V was consistent with Ag/AgCl reference before i-t testing (Fig. S18). These results confirmed the continuous catalytic and

structure stability of Mo₂C-L/Mo and Pt/Mo₂C-L/Mo at high current density, providing compelling evidence for the reliability of laser synthesis for stable electrocatalytic electrodes.

To confirm the synergistic effect and the role of the interface toward

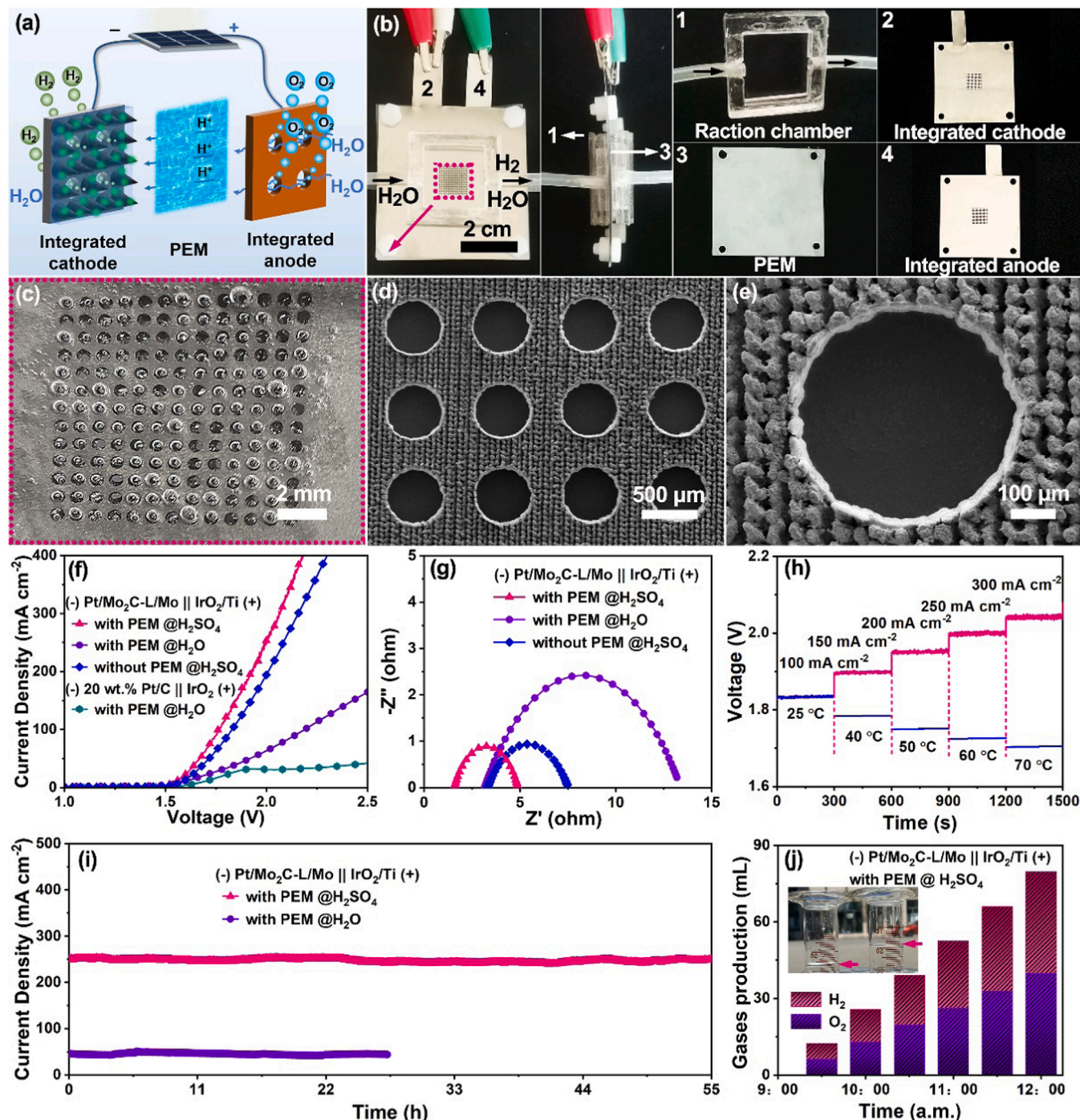


Fig. 5. (a) Illustration of the constructed proton exchange membrane water electrolyzer (PEMWE). (b) Digital image of the constructed PEMWE of (–) Pt/Mo₂C-L/Mo || IrO₂/Ti (+). (c) Digital image of the H₂ bubbles production from the porous structure of the integrated gas diffusion and catalytic electrode of Pt/Mo₂C-L/Mo. (d, e) SEM images of the integrated gas diffusion and catalytic electrode of Pt/Mo₂C-L/Mo. (f) Polarization curves of the constructed PEMWE of (–) Pt/Mo₂C-L/Mo || IrO₂/Ti (+) and (–) 20 wt.% Pt/C || IrO₂ (+) with and without PEM for overall water splitting in 0.5 M H₂SO₄ and H₂O. (g) Nyquist plots (overpotential of 500 mV) of the constructed PEMWE of (–) Pt/Mo₂C-L/Mo || IrO₂/Ti (+) with and without PEM for overall water splitting in 0.5 M H₂SO₄ and H₂O. (h) Chronopotentiometry curves of multi-current density process (the pink curves) and multi-temperature process at 100 mA cm^{–2} (the blue curves) of the constructed PEMWE of (–) Pt/Mo₂C-L/Mo || IrO₂/Ti (+) with PEM in 0.5 M H₂SO₄. (i) Current-time plots (voltage of 2.10 V) of the constructed PEMWE of (–) Pt/Mo₂C-L/Mo || IrO₂/Ti (+) with PEM in 0.5 M H₂SO₄ and H₂O. (j) The quantity of gases versus time of constructed PEMWE of (–) Pt/Mo₂C-L/Mo || IrO₂/Ti (+) with PEM in 0.5 M H₂SO₄ for solar-driven water splitting. Inset was the digital image of gases volume test by drainage method. (For interpretation of the references to colour in this figure legend, the reader is referred to the web version of this article.)

HER, density functional theory (DFT) calculations were conducted on Mo₂C (100), Pt cluster, and the interface between Mo₂C (100) and Pt cluster (Fig. 4g-h and S19). Commonly, an efficient HER catalyst had moderate hydrogen adsorption and the ΔG_{H^*} was closed to zero [61,62]. As shown in Fig. 4 h, the ΔG_{H^*} value of -0.05 eV on the interface between Mo₂C (100) and Pt cluster was close to zero. However, the strongly negative ΔG_{H^*} values of the Mo₂C (100) (-0.32 eV) and Pt cluster (-0.24 eV) were presented. Therefore, the interface between Mo₂C (100) and Pt cluster was more likely to be the effective HER catalytic sites. In addition, the HER activity of Pt/Mo₂C-L/Mo was compared with the reported Pt-based electrocatalysts. The overpotential at 10 mA cm^{-2} of Pt/Mo₂C-L/Mo was lower than the most of Pt-based electrocatalysts in previous reports (Fig. 4i and Table S1) [19,63–71]. Therefore, with the virtues of a low overpotential, small Tafel slope, and a favorable durability at high current density, the Pt/Mo₂C-L/Mo had great potential for practical application in hydrogen energy area.

3.5. Overall water splitting performance of the constructed PEMWE

Owing to the advantages of high current densities, low Ohmic loss, and fast system response and so on, the proton exchange membrane water electrolyzer (PEMWE) had been widely investigated and applied for the industrial area of the electrochemical water splitting [33,34]. Traditional PEMWE was comprised of cathode and anode collectors (electron transport), two porous transport layer (diffusion channel of gas and electrolyte), and membrane electrode (Pt/C-PEM-IrO₂), as shown in Fig. S20a. Herein, the laser synthesis in a mixed model afforded an alternative method for preparation of the integrated electrode composed of gas diffusion and catalytic layer, which simplified the structure of the PEMWE, as shown in Fig. 5a. Specifically, the Ti and Mo collectors with porous structure were obtained by a circular array mode of laser first, and acted as substrates for the synthesis of the integrated electrode of Pt/Mo₂C-L/Mo and IrO₂/Ti. The iridium dioxide particles on titanium foil (IrO₂/Ti) acted as anode electrode (synthesis details in Supporting Information), which morphology and crystal structure were proved by SEM image (Fig. S21a) and XRD pattern (Fig. S21b). The IrO₂/Ti showed efficient OER performance and stability in $0.5 \text{ M H}_2\text{SO}_4$ (Fig. S22). The photographs of simplified PEMWE of (–) Pt/Mo₂C-L/Mo || IrO₂/Ti (+) was shown in Fig. 5b, which was composed of reaction chambers, integrated cathode and anode, and PEM. The overall water splitting reaction was restricted in reaction chamber in which the electrolyte and gases were presented. The integrated electrodes of Pt/Mo₂C-L/Mo and IrO₂/Ti with periodic porous structure were acted as integrated cathode and anode, respectively. According measurement system equipping with a gas-liquid separator to purify the output hydrogen and a peristaltic pump to provide power for solution flow was constructed (Fig. S23). It was worth mentioning that the integrated electrode of Pt/Mo₂C-L/Mo with the pore structure and micropillars was multifunctional, which was simultaneously used for the current collection, electrolyte flow, gas diffusion, and catalytic layer. As shown in Fig. 5c, the H₂ bubbles emerged from the pore structure of the integrated gas diffusion and catalytic electrode of Pt/Mo₂C-L/Mo, indicating the periodic porous structure played a key role in gas diffusion. In order to exhibit the microstructure of the integrated gas diffusion and catalytic electrode of Pt/Mo₂C-L/Mo more clearly, the SEM images were shown in Fig. 5d, e. The pore structure with aperture diameter of $500 \mu\text{m}$ and hole pitch of $800 \mu\text{m}$ and the catalytic layer of Pt/Mo₂C-L/Mo micropillars were observed.

The concentration and diffusion distance of H⁺ protons played the important role in PEMWE. The H⁺ protons came from the $0.5 \text{ M H}_2\text{SO}_4$ in acid electrolyte or the strongly acidic groups ($-\text{SO}_3\text{H}$) on the surface of proton membrane in pure water. In addition, the diffusion distance of H⁺ protons were reduced by constructing the sandwich membrane electrode or introducing the acid electrolyte. Herein, the constructed PEMWE of (–) Pt/Mo₂C-L/Mo || IrO₂/Ti (+) with PEM in $0.5 \text{ M H}_2\text{SO}_4$ possessed the best performance of water splitting (Fig. 5f). The cell

voltage of the constructed PEMWE of (–) Pt/Mo₂C-L/Mo || IrO₂/Ti (+) with PEM was 1.55 V in $0.5 \text{ M H}_2\text{SO}_4$ at 10 mA cm^{-2} , which was lower than that of the PEMWE of (–) Pt/Mo₂C-L/Mo || IrO₂/Ti (+) with PEM in pure H₂O (1.59 V) and electrolyzer of (–) Pt/Mo₂C-L/Mo || IrO₂/Ti (+) without PEM in $0.5 \text{ M H}_2\text{SO}_4$ (1.58 V) (the illustration and photo as shown in Fig. S24). Due to the more sufficient H⁺ and shorter ion diffusion distance, the constructed PEMWE of (–) Pt/Mo₂C-L/Mo || IrO₂/Ti (+) with PEM in $0.5 \text{ M H}_2\text{SO}_4$ obtained the large current density of 122 mA cm^{-2} applying the voltage of 1.80 V . This current density was much larger than that of constructed PEMWE of (–) Pt/Mo₂C-L/Mo || IrO₂/Ti (+) with PEM in pure H₂O (33 mA cm^{-2}) and the electrolyzer of (–) Pt/Mo₂C-L/Mo || IrO₂/Ti (+) without PEM in $0.5 \text{ M H}_2\text{SO}_4$ (85 mA cm^{-2}). However, the commercial PEMWE of (–) 20 wt. % Pt/C || IrO₂ (+) only achieved 22 mA cm^{-2} at the voltage of 1.80 V , and the voltage was 1.69 V at 10 mA cm^{-2} . In order to study the ions transport and charge transfer in the electrolyzer, the Nyquist plots of (–) Pt/Mo₂C-L/Mo || IrO₂/Ti (+) with and without PEM for overall water splitting in $0.5 \text{ M H}_2\text{SO}_4$ and H₂O were obtained with overpotential of 500 mV (Fig. 5g). The series resistance (R_s) (1.6Ω) and charge transfer resistance (R_{ct}) (3.3Ω) of the constructed PEMWE of (–) Pt/Mo₂C-L/Mo || IrO₂/Ti (+) with PEM in $0.5 \text{ M H}_2\text{SO}_4$ were smaller than those of the constructed PEMWE of (–) Pt/Mo₂C-L/Mo || IrO₂/Ti (+) with PEM in H₂O ($R_s=3.2 \Omega$, $R_{ct}=10.0 \Omega$) and the electrolyzer of (–) Pt/Mo₂C-L/Mo || IrO₂/Ti (+) without PEM in $0.5 \text{ M H}_2\text{SO}_4$ ($R_s=3.3 \Omega$, $R_{ct}=4.2 \Omega$), which were due to the more sufficient H⁺ and shorter ions diffusion distance for electrolyzer with PEM in $0.5 \text{ M H}_2\text{SO}_4$. For the smaller of R_s , the ions transport in H₂SO₄ was faster than H₂O, and ions diffusion distance was decreased when the PEM was added. For the smaller of R_{ct} , the H⁺ protons came from both of the H₂SO₄ electrolyte and the strongly acidic groups ($-\text{SO}_3\text{H}$) on the surface of proton membrane, so the constructed PEMWE of (–) Pt/Mo₂C-L/Mo || IrO₂/Ti (+) with PEM in $0.5 \text{ M H}_2\text{SO}_4$ had the quicker reaction rate. Those results were consistent with the results of polarization curves (Fig. 5f).

For investigating the electrochemical durability, the multi-current density measurement of the constructed PEMWE of (–) Pt/Mo₂C-L/Mo || IrO₂/Ti (+) with PEM in $0.5 \text{ M H}_2\text{SO}_4$ was conducted by chronopotentiometry (Fig. 5h, the pink curve). The current density of multi-current density process was increasing from 100 mA cm^{-2} to 300 mA cm^{-2} . The result showed smooth change of the potential as the current density increasing from 100 to 300 mA cm^{-2} . In addition, the multi-temperature process was tested at 100 mA cm^{-2} for approaching practical industrial application conditions. As shown in the blue curves of Fig. 5h, the constructed PEMWE of (–) Pt/Mo₂C-L/Mo || IrO₂/Ti (+) with PEM operated favorable in $0.5 \text{ M H}_2\text{SO}_4$ electrolyte under high-temperature conditions at 25 , 40 , 50 , 60 , and 70°C . To further verify the durability of the constructed PEMWE of (–) Pt/Mo₂C-L/Mo || IrO₂/Ti (+), current-time measurements were performed in $0.5 \text{ M H}_2\text{SO}_4$ and H₂O (Fig. 5i). The i-t testing of the constructed PEMWE of (–) Pt/Mo₂C-L/Mo || IrO₂/Ti (+) were carried out with the voltage of 2.10 V in $0.5 \text{ M H}_2\text{SO}_4$ and pure H₂O for 55 h and 27 h , respectively. Their current densities were barely decayed ($\sim 100\%$ retention in $0.5 \text{ M H}_2\text{SO}_4$ and pure H₂O), explicitly indicating the excellent electrochemical stability, which were much better than that of PEMWE of (–) 20 wt. % Pt/C || IrO₂ (+) ($\sim 54\%$ retention) (Fig. S25a). The poor stability was more obvious in the electrolyzer of (–) 20 wt. % Pt/C || IrO₂ (+) without PEM to hold electrocatalysts, as shown in Fig. S26. The LSV curves before and after i-t testing of the PEMWE of (–) Pt/Mo₂C-L/Mo || IrO₂/Ti (+) in $0.5 \text{ M H}_2\text{SO}_4$ and pure H₂O had remained virtually unchanged (Fig. S25c, d). This was because that the strong bonding between Pt/Mo₂C-L and Mo substrate was presented for Pt/Mo₂C-L/Mo prepared by in-situ laser synthesis and processing, which avoided using Nafion adhesive to improve the structural stability of electrode in both PEMWE (Fig. 5a) and electrolyzer without PEM (Fig. S24a).

In order to further promoting the practicability of constructed PEMWE, a sustainable pathway to produce renewable fuels, solar-driven electrochemical water splitting system was established [72]. Herein,

the constructed PEMWE of (–) Pt/Mo₂C-L/Mo || IrO₂/Ti (+) with PEM driven by a solar cell for water splitting in 0.5 M H₂SO₄ was conducted outside in a very nice weather with an average temperature of 27 °C on August 25, 2021 in Jinan, Shandong Province, China (36°40' N, 117°00' E) and the digital image in testing process was shown in Fig. S27a. The high average H₂ and O₂ production rate of ~26.6 mL h⁻¹ and ~13.3 mL h⁻¹ was obtained by drainage method (Fig. S5j). The gases production rate versus time curves were exhibited in Fig. S27b, and the gases production rate had slight increased as the increase of time, which was because the closer it was to noon, the stronger the sunlight became. Those results confirmed that the constructed PEMWE of (–) Pt/Mo₂C-L/Mo || IrO₂/Ti (+) possessed the possible application in the solar-driven renewable fuel production.

4. Conclusions

A controllable laser synthesis strategy of large-sized Pt/Mo₂C-L/Mo electrode at ambient condition was proposed. The obtained Pt/Mo₂C-L/Mo had active electrocatalytic property for HER with the overpotential (η_{10}) of 21 mV and continuous stability (~100% retention for 100 h) at the high current density (1317 mA cm⁻²). This was due to the high active interface between Mo₂C and Pt, and the unique periodic structures of micropillars and pores. In addition, the constructed PEMWE of (–) Pt/Mo₂C-L/Mo || IrO₂/Ti (+) composed of integrated Pt/Mo₂C-L/Mo as cathode and IrO₂/Ti as anode delivered a high current density of 122 mA cm⁻² with the voltage of 1.80 V in 0.5 M H₂SO₄ for water splitting, which was much larger than the commercial PEMWE of (–) 20 wt.% Pt/C || IrO₂ (+) in H₂O (22 mA cm⁻²). The periodic porous structure of the integrated electrodes of Pt/Mo₂C-L/Mo for promoting gas and electrolyte diffusion, as well as the strategy in the increase of concentration and the reduction of diffusion distance of H⁺ protons played the important role in PEMWE of (–) Pt/Mo₂C-L/Mo || IrO₂/Ti (+) for the splendid water splitting performance. The universal laser synthesis method of active HER electrocatalysts and integrated electrodes with long-term stability at high current density in ambient environment have a bright application prospect in hydrogen energy area.

CRediT authorship contribution statement

Haifeng Yuan: Data curation, Formal analysis, Investigation, Visualization, Writing - original draft. **Lili Zhao:** Data curation, Funding acquisition, Methodology, Validation, Writing - review & editing. **Bin Chang:** Supervision, Validation. **Yuke Chen:** Formal analysis, Supervision. **Tianjiao Dong:** Supervision, Validation. **Jietong He:** Software, Validation. **Di Jiang:** Supervision, Validation. **Wanqiang Yu:** Supervision, Validation. **Hong Liu:** Project administration, Resources, Supervision, Validation. **Weijia Zhou:** Conceptualization, Funding acquisition, Project administration, Resources, Supervision, Writing - review & editing.

Declaration of Competing Interest

The authors declare that they have no known competing financial interests or personal relationships that could have appeared to influence the work reported in this paper.

Acknowledgements

This work was supported by the Taishan Scholars Project Special Funds (tsqn201812083); the Natural Science Foundation of Shandong Province (ZR2019YQ20, ZR2019BB001, ZR2021JQ15); Innovative Team Project of Jinan (2021GXRC019) and the National Natural Science Foundation of China (51972147, 51902132, 52022037).

Appendix A. Supporting information

Supplementary data associated with this article can be found in the online version at doi:10.1016/j.apcatb.2022.121455.

References

- [1] D. Li, X. Chen, Y. Lv, G. Zhang, Y. Huang, W. Liu, Y. Li, R. Chen, C. Nuckolls, H. Ni, An effective hybrid electrocatalyst for the alkaline HER: highly dispersed Pt sites immobilized by a functionalized NiRu-hydroxide, *Appl. Catal. B: Environ.* 269 (2020), 118824, <https://doi.org/10.1016/j.apcatb.2020.118824>.
- [2] P. Zhou, G. Zhai, X. Lv, Y. Liu, Z. Wang, P. Wang, Z. Zheng, H. Cheng, Y. Dai, B. Huang, Boosting the electrocatalytic HER performance of Ni₃N-V₂O₃ via the interface coupling effect, *Appl. Catal. B: Environ.* 283 (2021), 119590, <https://doi.org/10.1016/j.apcatb.2020.119590>.
- [3] B. Zhang, Y. Zheng, T. Ma, C. Yang, Y. Peng, Z. Zhou, M. Zhou, S. Li, Y. Wang, C. Cheng, Designing MOF nanoarchitectures for electrochemical water splitting, *Adv. Mater.* 33 (2021), 2006042, <https://doi.org/10.1002/adma.202006042>.
- [4] S. Choi, J. Kwon, S. Jo, S. Kim, K. Park, S. Kim, H. Han, U. Paik, T. Song, Highly efficient and stable bifunctional electrocatalysts with decoupled active sites for hydrogen evolution and oxygen reduction reactions, *Appl. Catal. B: Environ.* 298 (2021), 120530, <https://doi.org/10.1016/j.apcatb.2021.120530>.
- [5] C.-F. Du, X. Sun, H. Yu, W. Fang, Y. Jing, Y. Wang, S. Li, X. Liu, Q. Yan, V₄C₃T_x MXene: a promising active substrate for reactive surface modification and the enhanced electrocatalytic oxygen evolution activity, *InfoMat* 2 (2020) 950–959, <https://doi.org/10.1002/inf2.12078>.
- [6] Y. Men, Y. Tan, P. Li, X. Cao, S. Jia, J. Wang, S. Chen, W. Luo, Tailoring the 3d-orbital electron filling degree of metal center to boost alkaline hydrogen evolution electrocatalysis, *Appl. Catal. B: Environ.* 284 (2021), 119718, <https://doi.org/10.1016/j.apcatb.2020.119718>.
- [7] C. Zhang, X. Liang, R. Xu, C. Dai, B. Wu, G. Yu, B. Chen, X. Wang, N. Liu, H₂ in situ inducing strategy on Pt surface segregation over low Pt doped PtNi₅ nanoalloy with superhigh alkaline HER activity, *Adv. Funct. Mater.* 31 (2021), 2008298, <https://doi.org/10.1002/adfm.202008298>.
- [8] N. Yao, R. Meng, F. Wu, Z. Fan, G. Cheng, W. Luo, Oxygen-vacancy-induced CeO₂/Co₄N heterostructures toward enhanced pH-universal hydrogen evolution reactions, *Appl. Catal. B: Environ.* 277 (2020), 119282, <https://doi.org/10.1016/j.apcatb.2020.119282>.
- [9] X. Liang, L. Shi, R. Cao, G. Wan, W. Yan, H. Chen, Y. Liu, X. Zou, Perovskite-type solid solution nano-electrocatalysts enable simultaneously enhanced activity and stability for oxygen evolution, *Adv. Mater.* 32 (2020), 2001430, <https://doi.org/10.1002/adma.202001430>.
- [10] L. Zhou, S.-Y. Lu, S. Guo, Recent progress on precious metal single atom materials for water splitting catalysis, *SusMat* 1 (2021) 194–210, <https://doi.org/10.1002/sus2.15>.
- [11] J. Chen, M. Qin, S. Ma, R. Fan, X. Zheng, S. Mao, C. Chen, Y. Wang, Rational construction of Pt/PtTe_x interface with optimal intermediate adsorption energy for efficient hydrogen evolution reaction, *Appl. Catal. B: Environ.* 299 (2021), 120640, <https://doi.org/10.1016/j.apcatb.2021.120640>.
- [12] K. Eiler, S. Suriñach, J. Sort, E. Pellicer, Mesoporous Ni-rich Ni-Pt thin films: electrodeposition, characterization and performance toward hydrogen evolution reaction in acidic media, *Appl. Catal. B: Environ.* 265 (2020), 118597, <https://doi.org/10.1016/j.apcatb.2020.118597>.
- [13] D.V. Esposito, S.T. Hunt, A.L. Stottlmyer, K.D. Dobson, B.E. McCandless, R. W. Birkmire, J.G. Chen, Low-cost hydrogen-evolution catalysts based on monolayer platinum on tungsten monocarbide substrates, *Angew. Chem. Int. Ed.* 49 (2010) 9859–9862, <https://doi.org/10.1002/anie.201004718>.
- [14] M.A.R. Anjum, M.H. Lee, J.S. Lee, Boron- and nitrogen-codoped molybdenum carbide nanoparticles imbedded in a BCN network as a bifunctional electrocatalyst for hydrogen and oxygen evolution reactions, *ACS Catal.* 8 (2018) 8296–8305, <https://doi.org/10.1021/acsami.7b01096>.
- [15] D.S. Baek, G.Y. Jung, B. Seo, J.C. Kim, H.-W. Lee, T.J. Shin, H.Y. Jeong, S.K. Kwak, S.H. Joo, Ordered mesoporous metastable α -MoC_{1-x} with enhanced water dissociation capability for boosting alkaline hydrogen evolution activity, *Adv. Funct. Mater.* 29 (2019), 1901217, <https://doi.org/10.1002/adfm.201901217>.
- [16] D.V. Esposito, S.T. Hunt, Y.C. Kimmel, J.G. Chen, A new class of electrocatalysts for hydrogen production from water electrolysis: metal monolayers supported on low-cost transition metal carbides, *J. Am. Chem. Soc.* 134 (2012) 3025–3033, <https://doi.org/10.1021/ja208656v>.
- [17] Y. Gu, B. Wei, D. Legut, Z. Fu, S. Du, H. Zhang, J.S. Francisco, R. Zhang, Single atom-modified hybrid transition metal carbides as efficient hydrogen evolution reaction catalysts, *Adv. Funct. Mater.* 31 (2021), 2104285, <https://doi.org/10.1002/adfm.202104285>.
- [18] O.T. Ajenifujah, A. Nouralishahi, S. Carl, S.C. Eady, Z. Jiang, L.T. Thompson, Platinum supported on early transition metal carbides: efficient electrocatalysts for methanol electro-oxidation reaction in alkaline electrolyte, *Chem. Eng. J.* 406 (2021), 126670, <https://doi.org/10.1016/j.cej.2020.126670>.
- [19] H.J. Song, M.-C. Sung, H. Yoon, B. Ju, D.-W. Kim, Ultrafine α -phase molybdenum carbide decorated with platinum nanoparticles for efficient hydrogen production in acidic and alkaline media, *Adv. Sci.* 6 (2019), 1802135, <https://doi.org/10.1002/advs.201802135>.
- [20] Y. Qiu, Z. Wen, C. Jiang, X. Wu, R. Si, J. Bao, Q. Zhang, L. Gu, J. Tang, X. Guo, Rational design of atomic layers of Pt anchored on Mo₂C nanorods for efficient

- hydrogen evolution over a wide pH range, *Small* 15 (2019), 1900014, <https://doi.org/10.1002/smll.201900014>.
- [21] S.H. Joo, J.S. Lee, Metal carbides as alternative electrocatalysts for energy conversion reactions, *J. Catal.* 404 (2021) 911–924, <https://doi.org/10.1016/j.jcat.2021.07.013>.
- [22] Y. Liu, T.G. Kelly, J.G. Chen, W.E. Mustain, Metal carbides as alternative electrocatalyst supports, *ACS Catal.* 3 (2013) 1184–1194, <https://doi.org/10.1021/cs4001249>.
- [23] J. Jia, W. Zhou, Z. Wei, T. Xiong, G. Li, L. Zhao, X. Zhang, H. Liu, J. Zhou, S. Chen, Molybdenum carbide on hierarchical porous carbon synthesized from Cu-MoO₂ as efficient electrocatalysts for electrochemical hydrogen generation, *Nano Energy* 41 (2017) 749–757, <https://doi.org/10.1016/j.nanoen.2017.10.030>.
- [24] X. Zhao, W. Sun, D. Geng, W. Fu, J. Dan, Y. Xie, P.R.C. Kent, W. Zhou, S. J. Pennycook, K.P. Loh, Edge segregated polymorphism in 2D molybdenum carbide, *Adv. Mater.* 31 (2019), 1808343, <https://doi.org/10.1002/adma.201808343>.
- [25] T. Li, W. Luo, H. Kitadai, X. Wang, X. Ling, Probing the domain architecture in 2D α -Mo₂C via polarized raman spectroscopy, *Adv. Mater.* 31 (2019), 1807160, <https://doi.org/10.1002/adma.201807160>.
- [26] Z. Li, J.-Y. Fu, Y. Feng, C.-K. Dong, H. Liu, X.-W. Du, A silver catalyst activated by stacking faults for the hydrogen evolution reaction, *Nat. Catal.* 2 (2019) 1107–1114, <https://doi.org/10.1038/s41929-019-0365-9>.
- [27] R.C. Forsythe, C.P. Cox, M.K. Wilsey, A.M. Müller, Pulsed laser in liquids made nanomaterials for catalysis, *Chem. Rev.* 121 (2021) 7568–7637, <https://doi.org/10.1021/acs.chemrev.0c01069>.
- [28] Y. Peng, J. Cao, J. Yang, W. Yang, C. Zhang, X. Li, R.A.W. Dryfe, L. Li, I.A. Kinloch, Z. Liu, Laser assisted solution synthesis of high performance graphene supported electrocatalysts, *Adv. Funct. Mater.* 30 (2020), 2001756, <https://doi.org/10.1002/adfm.202001756>.
- [29] Y.-J. Tang, H. Zheng, Y. Wang, W. Zhang, K. Zhou, Laser-induced annealing of metal-organic frameworks on conductive substrates for electrochemical water splitting, *Adv. Funct. Mater.* 31 (2021), 2102648, <https://doi.org/10.1002/adfm.202102648>.
- [30] X. Zhang, C. Jian, T. Zhu, Z. Fan, W. Wang, M. Wei, B. Li, M. Folmar Diaz, P. Ashby, Z. Lu, Y. Chu, Z. Wang, X. Ding, Y. Xie, J. Chen, J.N. Hohman, M. Sanghadasa, J. C. Grossman, L. Lin, Laser-sculptured ultrathin transition metal carbide layers for energy storage and energy harvesting applications, *Nat. Commun.* 10 (2019) 3112, <https://doi.org/10.1038/s41467-019-10999-z>.
- [31] L. Zhao, Z. Liu, D. Chen, F. Liu, Z. Yang, X. Li, H. Yu, H. Liu, W. Zhou, Laser synthesis and microfabrication of micro/nanostructured materials toward energy conversion and storage, *Nano-Micro Lett.* 13 (2021) 49, <https://doi.org/10.1007/s40820-020-00577-0>.
- [32] P. Fan, H. Wu, M. Zhong, H. Zhang, B. Bai, G. Jin, Large-scale cauliflower-shaped hierarchical copper nanostructures for efficient photothermal conversion, *Nanoscale* 8 (2016) 14617–14624, <https://doi.org/10.1039/C6NR03662G>.
- [33] Z.L. Zhao, Q. Wang, X. Huang, Q. Peng, S. Gu, Z. Zhang, H. Xu, L. Zeng, M. Gu, H. Li, Boosting the oxygen evolution reaction using defect-rich ultra-thin ruthenium oxide nanosheets in acidic media, *Energy Environ. Sci.* 13 (2020) 5143–5151, <https://doi.org/10.1039/D0EE01960G>.
- [34] Z. Li, J.-Y. Fu, Y. Feng, C.-K. Dong, H. Liu, X.-W. Du, A review of proton exchange membrane water electrolysis on degradation mechanisms and mitigation strategies, *J. Power Sources* 366 (2017) 33–55, <https://doi.org/10.1016/j.jpowsour.2017.09.006>.
- [35] P.T. Nguyen, J. Jang, Y. Lee, S.T. Choi, J.B. In, Laser-assisted fabrication of flexible monofilament fiber supercapacitors, *J. Mater. Chem. A* 9 (2021) 4841–4850, <https://doi.org/10.1039/D0TA10283K>.
- [36] M. Xiao, Z. Zheng, D. Shen, W.W. Duley, Y.N. Zhou, Laser-induced joining of nanoscale materials: processing, properties, and applications, *Nano Today* 35 (2020), 100959, <https://doi.org/10.1016/j.nantod.2020.100959>.
- [37] H. Yuan, F. Liu, G. Xue, H. Liu, Y. Wang, Y. Zhao, X. Zhang, L. Zhao, Z. Liu, H. Liu, W. Zhou, Laser patterned and bifunctional Ni@N-doped carbon nanotubes as electrocatalyst and photothermal conversion layer for water splitting driven by thermoelectric device, *Appl. Catal. B: Environ.* 283 (2021), 119647, <https://doi.org/10.1016/j.apcatb.2020.119647>.
- [38] G. Kresse, J. Furthmüller, Efficient iterative schemes for ab initio total-energy calculations using a plane-wave basis set, *Phys. Rev. B* 54 (1996) 11169–11186, <https://doi.org/10.1103/PhysRevB.54.11169>.
- [39] G. Kresse, D. Joubert, From ultrasoft pseudopotentials to the projector augmented-wave method, *Phys. Rev. B* 59 (1999) 1758–1775, <https://doi.org/10.1103/PhysRevB.59.1758>.
- [40] P.E. Blöchl, Projector augmented-wave method, *Phys. Rev. B* 50 (1994) 17953–17979, <https://doi.org/10.1103/PhysRevB.50.17953>.
- [41] J.P. Perdew, J.A. Chevary, S.H. Vosko, K.A. Jackson, M.R. Pederson, D.J. Singh, C. Fiolhais, Atoms, molecules, solids, and surfaces: applications of the generalized gradient approximation for exchange and correlation, *Phys. Rev. B* 46 (1992) 6671–6687, <https://doi.org/10.1103/PhysRevB.46.6671>.
- [42] J.P. Perdew, Y. Wang, Accurate and simple analytic representation of the electron-gas correlation energy, *Phys. Rev. B* 45 (1992) 13244–13249, <https://doi.org/10.1103/physrevb.45.13244>.
- [43] J.K. Noerskov, T. Bligaard, A. Logadottir, J.R. Kitchin, J.G. Chen, S. Pandalov, U. Stimming, Trends in the exchange current for hydrogen evolution, *ChemInform* 36 (2005) J23–J26, <https://doi.org/10.1002/chin.200524023>.
- [44] Y. Huang, J. Hu, H. Xu, W. Bian, J. Ge, D. Zang, D. Cheng, Y. Lv, C. Zhang, J. Gu, Y. Wei, Fine tuning electronic structure of catalysts through atomic engineering for enhanced hydrogen evolution, *Adv. Energy Mater.* 8 (2018), 1800789, <https://doi.org/10.1002/aenm.201800789>.
- [45] H. Cheng, L.-X. Ding, G.-F. Chen, L. Zhang, J. Xue, H. Wang, Molybdenum carbide nanodots enable efficient electrocatalytic nitrogen fixation under ambient conditions, *Adv. Mater.* 30 (2018), 1803694, <https://doi.org/10.1002/adma.201803694>.
- [46] K. Xia, J. Guo, C. Xuan, T. Huang, Z. Deng, L. Chen, D. Wang, Ultrafine molybdenum carbide nanoparticles supported on nitrogen doped carbon nanosheets for hydrogen evolution reaction, *Chin. Chem. Lett.* 30 (2019) 192–196, <https://doi.org/10.1016/j.ccl.2018.05.009>.
- [47] Y. Chen, S. Ji, W. Sun, Y. Lei, Q. Wang, A. Li, W. Chen, G. Zhou, Z. Zhang, Y. Wang, L. Zheng, Q. Zhang, L. Gu, X. Han, D. Wang, Y. Li, Engineering the atomic interface with single platinum atoms for enhanced photocatalytic hydrogen production, *Angew. Chem. Int. Ed.* 59 (2020) 1295–1301, <https://doi.org/10.1002/anie.201912439>.
- [48] L. Lin, W. Zhou, R. Gao, S. Yao, X. Zhang, W. Xu, S. Zheng, Z. Jiang, Q. Yu, Y.-W. Li, C. Shi, X.-D. Wen, D. Ma, Low-temperature hydrogen production from water and methanol using Pt/ α -MoC catalysts, *Nature* 544 (2017) 80–83, <https://doi.org/10.1038/nature21672>.
- [49] S. Saha, B. Martin, B. Leonard, D. Li, Probing synergistic effects between platinum nanoparticles deposited via atomic layer deposition and a molybdenum carbide nanotube support through surface characterization and device performance, *J. Mater. Chem. A* 4 (2016) 9253–9265, <https://doi.org/10.1039/C6TA03198F>.
- [50] Z. Zhao, C. Chen, Z. Liu, J. Huang, M. Wu, H. Liu, Y. Li, Y. Huang, Pt-based nanocrystal for electrocatalytic oxygen reduction, *Adv. Mater.* 31 (2019), 1808115, <https://doi.org/10.1002/adma.201808115>.
- [51] Z. Wang, H. Luo, R. Lin, H. Lei, Y. Yuan, Z. Zhu, X. Li, W. Mai, Theoretical calculation guided electrocatalysts design: nitrogen saturated porous Mo₂C nanostructures for hydrogen production, *Appl. Catal. B: Environ.* 257 (2019), 117891, <https://doi.org/10.1016/j.apcatb.2019.117891>.
- [52] J. Liu, B. Chen, Y. Kou, Z. Liu, X. Chen, Y. Li, Y. Deng, X. Han, W. Hu, C. Zhong, Pt-decorated highly porous flower-like Ni particles with high mass activity for ammonia electro-oxidation, *J. Mater. Chem. A* 4 (2016) 11060–11068, <https://doi.org/10.1039/C6TA02284G>.
- [53] J. He, Z. Cui, S. Zhu, Z. Li, S. Wu, L. Zheng, Z. Gao, Y. Liang, Insight into the electrochemical-cycling activation of Pt/molybdenum carbide toward synergistic hydrogen evolution catalysis, *J. Catal.* 384 (2020) 169–176, <https://doi.org/10.1016/j.jcat.2020.02.020>.
- [54] M. Cai, W. Liu, X. Luo, C. Chen, R. Pan, H. Zhang, M. Zhong, Three-dimensional and in situ-activated spinel oxide nanoporous clusters derived from stainless steel for efficient and durable water oxidation, *ACS Appl. Mater. Interfaces* 12 (2020) 13971–13981, <https://doi.org/10.1021/acsami.0c00701>.
- [55] W. Zhou, J. Jia, J. Lu, L. Yang, D. Hou, G. Li, S. Chen, Recent developments of carbon-based electrocatalysts for hydrogen evolution reaction, *Nano Energy* 28 (2016) 29–43, <https://doi.org/10.1016/j.nanoen.2016.08.027>.
- [56] H. Chen, X. Liang, Y. Liu, X. Ai, T. Asefa, X. Zou, Active site engineering in porous electrocatalysts, *Adv. Mater.* 32 (2020), 2002435, <https://doi.org/10.1002/adma.202002435>.
- [57] L. Huang, D. Chen, G. Luo, Y.-R. Lu, C. Chen, Y. Zou, C.-L. Dong, Y. Li, S. Wang, Zirconium-regulation-induced bifunctionality in 3D cobalt-iron oxide nanosheets for overall water splitting, *Adv. Mater.* 31 (2019), 1901439, <https://doi.org/10.1002/adma.201901439>.
- [58] L. Yang, L. Zeng, H. Liu, Y. Deng, Z. Zhou, J. Yu, H. Liu, W. Zhou, Hierarchical mesosphere of MoNi porous nanosheets as electrocatalyst and cocatalyst for hydrogen evolution reaction, *Appl. Catal. B: Environ.* 249 (2019) 98–105, <https://doi.org/10.1016/j.apcatb.2019.02.062>.
- [59] G. Li, J. Wang, J. Yu, H. Liu, Q. Cao, J. Du, L. Zhao, J. Jia, H. Liu, W. Zhou, Ni-Ni₃P nanoparticles embedded into N, P-doped carbon on 3D graphene frameworks via in situ phosphatization of saccharomycetes with multifunctional electrodes for electrocatalytic hydrogen production and anodic degradation, *Appl. Catal. B: Environ.* 261 (2020), 118147, <https://doi.org/10.1016/j.apcatb.2019.118147>.
- [60] J. Wang, X. Ge, Z. Liu, L. Thia, Y. Yan, W. Xiao, X. Wang, Heterogeneous electrocatalyst with molecular cobalt ions serving as the center of active sites, *J. Am. Chem. Soc.* 139 (2017) 1878–1884, <https://doi.org/10.1021/jacs.6b10307>.
- [61] X. Li, J. Yu, J. Jia, A. Wang, L. Zhao, T. Xiong, H. Liu, W. Zhou, Confined distribution of platinum clusters on MoO₂ hexagonal nanosheets with oxygen vacancies as a high-efficiency electrocatalyst for hydrogen evolution reaction, *Nano Energy* 62 (2019) 127–135, <https://doi.org/10.1016/j.nanoen.2019.05.013>.
- [62] X. Liu, K. Ni, C. Niu, R. Guo, W. Xi, Z. Wang, J. Meng, J. Li, Y. Zhu, P. Wu, Q. Li, J. Luo, X. Wu, L. Mai, Upraising the O 2p orbital by integrating Ni with MoO₂ for accelerating hydrogen evolution kinetics, *ACS Catal.* 9 (2019) 2275–2285, <https://doi.org/10.1021/acscatal.8b04817>.
- [63] H. Wei, H. Wu, K. Huang, B. Ge, J. Ma, J. Lang, D. Zu, M. Lei, Y. Yao, W. Guo, H. Wu, Ultra-low-temperature photochemical synthesis of atomically dispersed Pt catalysts for the hydrogen evolution reaction, *Chem. Sci.* 10 (2019) 2830–2836, <https://doi.org/10.1039/C8SC04986F>.
- [64] L. Liang, H. Jin, H. Zhou, B. Liu, C. Hu, D. Chen, Z. Wang, Z. Hu, Y. Zhao, H.-W. Li, D. He, S. Mu, Cobalt single atom site isolated Pt nanoparticles for efficient ORR and HER in acid media, *Nano Energy* 88 (2021), 106221, <https://doi.org/10.1016/j.nanoen.2021.106221>.
- [65] P. Kuang, Y. Wang, B. Zhu, F. Xia, C.-W. Tung, J. Wu, H.M. Chen, J. Yu, Pt single atoms supported on N-doped mesoporous hollow carbon spheres with enhanced electrocatalytic H₂-evolution activity, *Adv. Mater.* 33 (2021), 2008599, <https://doi.org/10.1002/adma.202008599>.
- [66] Y. Shi, Z.-R. Ma, Y.-Y. Xiao, Y.-C. Yin, W.-M. Huang, Z.-C. Huang, Y.-Z. Zheng, F.-Y. Mu, R. Huang, G.-Y. Shi, Y.-Y. Sun, X.-H. Xia, W. Chen, Electronic metal-support interaction modulates single-atom platinum catalysis for hydrogen evolution

- reaction, *Nat. Commun.* 12 (2021) 3021, <https://doi.org/10.1038/s41467-021-23306-6>.
- [67] C. Li, L. Zhang, Y. Zhang, Y. Zhou, J. Sun, X. Ouyang, X. Wang, J. Zhu, Y. Fu, PtRu alloy nanoparticles embedded on C₂N nanosheets for efficient hydrogen evolution reaction in both acidic and alkaline solutions, *Chem. Eng. J.* 428 (2022), 131085, <https://doi.org/10.1016/j.cej.2021.131085>.
- [68] X. Cheng, Y. Lu, L. Zheng, Y. Cui, M. Niibe, T. Tokushima, H. Li, Y. Zhang, G. Chen, S. Sun, J. Zhang, Charge redistribution within platinum-nitrogen coordination structure to boost hydrogen evolution, *Nano Energy* 73 (2020), 104739, <https://doi.org/10.1016/j.nanoen.2020.104739>.
- [69] Q. Dang, Y. Sun, X. Wang, W. Zhu, Y. Chen, F. Liao, H. Huang, M. Shao, Carbon dots-Pt modified polyaniline nanosheet grown on carbon cloth as stable and high-efficient electrocatalyst for hydrogen evolution in pH-universal electrolyte, *Appl. Catal. B: Environ.* 257 (2019), 117905, <https://doi.org/10.1016/j.apcatb.2019.117905>.
- [70] J. Xu, C. Zhang, H. Liu, J. Sun, R. Xie, Y. Qiu, F. Lü, Y. Liu, L. Zhuo, X. Liu, J. Luo, Amorphous MoO_x-stabilized single platinum atoms with ultrahigh mass activity for acidic hydrogen evolution, *Nano Energy* 70 (2020), 104529, <https://doi.org/10.1016/j.nanoen.2020.104529>.
- [71] J. Ji, Y. Zhang, L. Tang, C. Liu, X. Gao, M. Sun, J. Zheng, M. Ling, C. Liang, Z. Lin, Platinum single-atom and cluster anchored on functionalized MWCNTs with ultrahigh mass efficiency for electrocatalytic hydrogen evolution, *Nano Energy* 63 (2019), 103849, <https://doi.org/10.1016/j.nanoen.2019.06.045>.
- [72] Y. Zhong, Y. Lu, Z. Pan, J. Yang, G. Du, J. Chen, Q. Zhang, H. Zhou, J. Wang, C. Wang, W. Li, Efficient water splitting system enabled by multifunctional platinum-free electrocatalysts, *Adv. Funct. Mater.* 31 (2021), 2009853, <https://doi.org/10.1002/adfm.202009853>.